MOF-Derived CoSe₂@N-Doped Carbon Matrix Confined in Hollow Mesoporous Carbon Nanospheres as High-Performance Anodes for Potassium-Ion Batteries

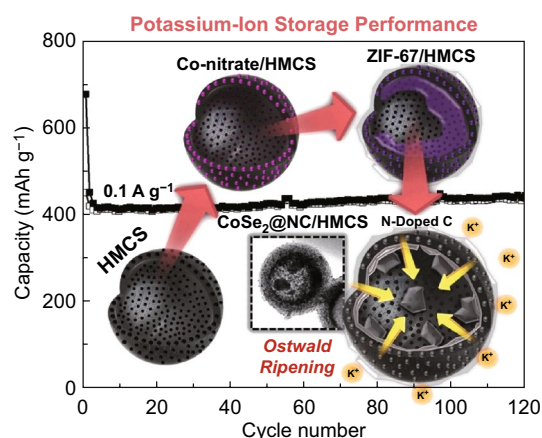Su Hyun Yang[1], Seung-Keun Park[2], Yun Chan Kang[1] ✉

HIGHLIGHTS

- A novel vacuum-assisted strategy is proposed to form N-doped carbon-encapsulated CoSe₂ nanocrystals within hollow mesoporous carbon nanospheres (CoSe₂@NC/HMCS) via a solid-state reaction.

- The "dual confinement" by both the N-doped carbon matrix derived from 2-methylimidazole and the small-sized pores of the hollow mesoporous carbon nanospheres can effectively prevent the overgrowth of CoSe₂ nanocrystals.

- CoSe₂@NC/HMCS exhibits an excellent electrochemical performance as the anode material for KIBs in terms of cycling stability and rate capability.

ABSTRACT In this work, a novel vacuum-assisted strategy is proposed to homogenously form Metal–organic frameworks within hollow mesoporous carbon nanospheres (HMCSs) via a solid-state reaction. The method is applied to synthesize an ultrafine CoSe₂ nanocrystal@N-doped carbon matrix confined within HMCSs (denoted as CoSe₂@NC/HMCS) for use as advanced anodes in high-performance potassium-ion batteries (KIBs). The approach involves a solvent-free thermal treatment to form a Co-based zeolitic imidazolate framework (ZIF-67) within the HMCS templates under vacuum conditions and the subsequent selenization. Thermal treatment under vacuum facilitates the infiltration of the cobalt precursor and organic linker into the HMCS and simultaneously transforms them into stable ZIF-67 particles without any solvents. During the subsequent selenization process, the "dual confinement system", composed of both the N-doped carbon matrix derived from the organic linker and the small-sized pores of HMCS, can effectively suppress the overgrowth of CoSe₂ nanocrystals. Thus, the resulting uniquely structured composite exhibits a stable cycling performance (442 mAh g⁻¹ at 0.1 A g⁻¹ after 120 cycles) and excellent rate capability (263 mAh g⁻¹ at 2.0 A g⁻¹) as the anode material for KIBs.

KEYWORDS Metal–organic frameworks; Hollow mesoporous carbon nanospheres; Potassium-ion batteries; Cobalt selenides; Electrode materials

Su Hyun Yang and Seung-Keun Park contributed equally to this work.

✉ Yun Chan Kang, yckang@korea.ac.kr

1 Department of Materials Science and Engineering, Korea University, Anam-Dong, Seongbuk-Gu, Seoul 136-713, Republic of Korea
2 Department of Chemical Engineering, Kongju National University, 1223-24 Cheonan-daero, Seobuk-gu, Cheonan 31080, Republic of Korea

1 Introduction

Potassium-ion batteries (KIBs) have recently attracted considerable attention for their high energy densities and the abundant availability of potassium as a raw material [1–3]. Thus, KIBs are being positioned as an alternative energy storage system to lithium-ion batteries (LIBs), which are currently the dominant power sources for electric vehicles and portable electronic devices. Nevertheless, the large radius of K^+ ions (1.38 Å) leads to a sluggish ion diffusion rate and large volume expansion of the electrode materials during repeated charge–discharge processes, which can hinder KIB commercialization [4, 5]. Therefore, the major challenge for KIBs resides in designing novel electrode materials with improved electrochemical performances, including high specific capacity, long cycling life, and excellent rate capability.

As emerging anode materials for KIBs, transition metal selenides have been intensively studied in consideration of their high specific theoretical capacities and narrow band-gap semiconductor properties [6, 7]. However, two major obstacles still require to be overcome: their large volume expansion upon potassiation and their low electrical conductivity. Thus, to enhance the potassium storage performance of transition metal selenides, many studies have proposed various strategies such as designing unique nanostructured materials and combining them with conductive carbonaceous materials [8–11].

Metal–organic frameworks (MOFs), consisting of metal cation nodes and organic struts, have been considered as ideal templates to synthesize diverse electrode materials owing to their tunable compositions and structures [12, 13]. In particular, upon pyrolysis under inert conditions, the metal cations contained in the MOFs can transform into metallic nanoparticles, which are simultaneously enclosed by the carbon matrix, resulting from the carbonization of the organic struts. By exploiting these features and controlling the atmospheric environment, researchers have obtained various metal compounds such as oxides, sulfides, and selenides embedded in the carbon matrix from MOF templates, and these compounds have been extensively applied as electrode materials for Li- and Na-ion batteries [14–17]. However, only a few studies have applied MOF-based composite to KIBs, and the resulting materials have not thus far afforded a satisfactory electrochemical performance [18–20].

Meanwhile, hollow or porous carbon templates are considered desirable substrates to endow various nanomaterials with structural robustness and electrical conductivity [21, 22]. Thus, several recent studies have suggested confining MOFs within these carbon templates to obtain enhanced structural stability and electrochemical properties [23–25]. However, although most of these studies used a well-known liquid-phase process for synthesizing MOFs, it is difficult to confine the MOF nanoparticles within the carbon templates with this method. As a result, some particles may be individually formed outside the templates, which can degrade the electrochemical performance. Therefore, the current challenge is to develop a new strategy for uniform MOF formation within the carbon templates to enhance the potassium-ion storage properties.

In this study, for the first time to the best of our knowledge, we propose a novel vacuum-assisted strategy to homogenously form MOFs within hollow mesoporous carbon nanospheres (HMCSs) via a solid-state reaction. Applying this method, we successfully synthesize an ultrafine $CoSe_2$-nanocrystal@N-doped carbon matrix confined within HMCSs (denoted as $CoSe_2$@NC/HMCS) for application as advanced anodes in high-performance KIBs. This approach involves a solvent-free thermal treatment to form a Co-based zeolitic imidazolate framework (ZIF-67) within HMCS templates under vacuum conditions, followed by selenization. The thermal treatment under vacuum facilitates both the infiltration of the cobalt precursor and 2-methylimidazole (2-MIM) into the HMCS and their simultaneous transformation into stable ZIF-67 particles without requiring any solvents. During the subsequent selenization process under a H_2/Ar atmosphere, the "dual confinement" by both the N-doped carbon matrix derived from 2-MIM and the small-sized pores of the HMCS can effectively prevent the overgrowth of $CoSe_2$ nanocrystals. Consequently, tiny $CoSe_2$ nanocrystals embedded in the N-doped carbon matrix are homogeneously distributed within the HMCSs. The resulting uniquely structured composite provides a conductive pathway for electrons and enable fast ion diffusion and easy accessibility of the electrolyte through ample pores. Moreover, the volume expansion of $CoSe_2$ is effectively suppressed during the electrochemical reaction. Thus, $CoSe_2$@NC/HMCS exhibits an excellent electrochemical performance as the anode material for KIBs in terms of cycling stability and rate capability. We also investigate the charge–discharge

mechanism of the electrode by applying various analytic tools.

2 Experimental Section

The CoSe$_2$@NC/HMCS composite was prepared through a two-step process composed of the formation of ZIF-67 nanoparticles within HMCSs via a solid-state reaction and subsequent selenization under a reducing atmosphere.

Firstly, HMCSs were synthesized as a conductive template according to previously reported methods [26]. The obtained 0.02 g of HMCSs was mixed with 0.2 mmol of Co(NO$_3$)$_2$·6H$_2$O (97%, SAMCHUN) with the use of ethanol solvents. After drying, the sample was heat-treated at 60 °C under vacuum for 12 h with a ramping rate of 2 °C min^{-1}. To form the ZIF-67 nanoparticles within HMCSs by means of the solid-state reaction, the cobalt-nitrate-loaded HMCSs were mixed with 2-MIM powder and heat-treated at 180 °C under vacuum for 1 h at a ramping rate of 10 °C min^{-1}. Subsequently, the synthesized ZIF-67@HMCS composite was washed by filtration with ethanol several times to remove the unreacted 2-MIM. Finally, CoSe$_2$@NC/HMCS composite was obtained via the selenization process of ZIF-67@HMCSs at 350 °C under a H$_2$/Ar atmosphere for 6 h. For comparison, the composite of CoSe$_2$ and HMCSs (denoted as CoSe$_2$/HMCS) was prepared by means of a process similar to that for CoSe$_2$@NC/HMCS composite except for 2-MIM addition. The experimental procedures for the characterization of the synthesized samples are described in detail in the Electronic Supplementary Material.

3 Results and Discussion

3.1 Synthesis and Characterization of CoSe$_2$@NC/HMCS and CoSe$_2$/HMCS Composites

The procedure for synthesizing the uniquely structured CoSe$_2$@NC/HMCS and CoSe$_2$/HMCS composites is schematically depicted in Scheme 1. Firstly, HMCSs with a central void and mesoporous shell are prepared as a nanoreactor for confining CoSe$_2$ nanocrystals (Scheme 1-①). Next, we use a vacuum-assisted infiltration method for the complete loading of MOFs into the HMCS templates. In particular, the powder obtained from drying the alcoholic solution containing Co(NO$_3$)$_2$·6H$_2$O and HMCSs is heat-treated at a temperature over the melting point of Co(NO$_3$)$_2$·6H$_2$O (55 °C) under vacuum (Scheme 1a-②). During this process, the melted Co-nitrate can easily infiltrate the well-developed mesopores of HMCS with vacuum assistance. Subsequently, a mixture of the Co-nitrate-infiltrated HMCSs and 2-MIM powder is further heated under vacuum (Scheme 1a-③) at a temperature of 180 °C, which is higher than the melting point of 2-MIM (145 °C). In this step, the thermal treatment under vacuum facilitates both the infiltration of 2-MIM into the HMCS and the simultaneous transformation of the mixture of the Co-nitrate and 2-MIM into stable ZIF-67 particles without requiring any solvent. During the subsequent
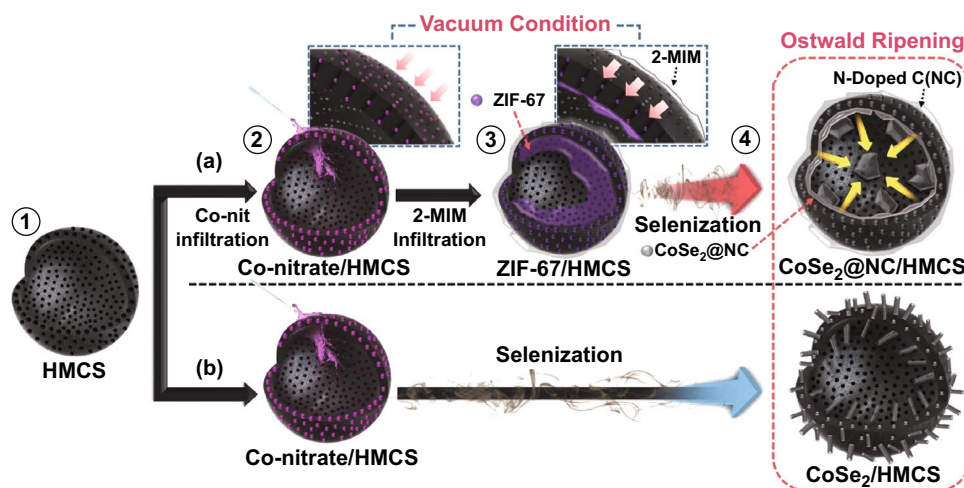
Scheme 1 Schematic illustration for the preparation of CoSe$_2$@NC/HMCS and CoSe$_2$/HMCS composites

selenization of ZIF-67/HMCS composite under H_2/Ar conditions, the Co ions contained in the ZIF-67 can transform into $CoSe_2$ nanoparticles, which are straightforwardly enclosed by the N-doped carbon matrix formed from the carbonization of 2-MIM, finally resulting in the formation of $CoSe_2$@ NC confined in HMCSs (Scheme 1a-④). For comparison purposes, we also synthesized $CoSe_2$/HMCS composite through the direct selenization of Co-nitrate/HMCSs, as illustrated in Scheme 1b. We note that due to the Ostwald ripening phenomenon, most $CoSe_2$ crystals protrude from the inner region of HMCSs to the outer surface, and they exhibit the shape of irregular rods or spheres.

The morphology and crystal structure changes of the samples obtained at each step were studied by means of various analytical tools. We note from Fig. S1a, b that the initially obtained monodisperse HMCSs exhibit not only numerous tiny pores on their 52-nm-thick shells but also a central void with a diameter of 330 nm; these plentiful pores and void can act as sites to effectively store the precursors. Via the vacuum-assisted method, the mesopores can be filled with Co-nitrate and 2-MIM precursors, a part of which is also deposited on the inner wall of the HMCS shell. Indeed, as confirmed from the scanning electron microscopy (SEM) and transmission electron microscopy (TEM) images (Figs. S1c–f and S2), the morphologies of the Co-nitrate/HMCS and ZIF-67/HMCS composites are very similar to that of the HMCS, and no aggregation is observed. Even after precursor loading, the central void of most HMCS can still clearly be discerned from the distinct contrast between the center and the edges, but with the HMCS shell becoming thicker (Figs. S1d, f, and S2a, b). The elemental mapping images in Fig. S2c depict the uniform distribution of C, N, and Co elements in the edge region of the shell, which indicates the formation of ZIF-67 on the inner surface of the HMCS shell. Furthermore, no peaks corresponding to ZIF-67 are observed in the X-ray diffraction (XRD) pattern of ZIF-67/ HMCS, whereas the sample obtained from the solid-state reaction between only Co-nitrate and 2-MIM in the same weight ratio clearly shows the corresponding peaks (Fig. S3). These results prove that the ZIF-67 nanoparticles can be suitably confined in the HMCS templates via the vacuum-assisted method.

In order to demonstrate the difficulty in confining the MOF nanoparticles within the carbon templates with liquid-phase process, we newly prepared ZIF-67/HMCS composite via a liquid-phase process, and as shown in Fig. S4a, b, most

of ZIF-67 nanoparticles were individually observed outside the HMCS template, which is quite different from the image of ZIF-67/HMCS composite prepared via a solid-state process. In light of these results, we believe that this solid-state process is an effective method to confine MOFs within the carbon templates. Also, we note that when the vacuum system is not used, some precursors cannot penetrate into inside and remain on the surface of HMCS as shown in Figs. S5 and S6 (SEM and TEM images). In particular, the sequential loading of Co-nitrate (Fig. S5a, b) and 2-MIM without applying vacuum leads to the formation of small-sized ZIF-67 nanoparticles on the outside of the HMCS (Figs. S5c, d, enlarged image, and S6a, b). The elemental mapping images in Fig. S6c depict the non-uniform distribution of C, N, and Co elements in the edge region of the shell, which revealed that the Co-nitrate and 2-MIM precursors cannot penetrate into HMCS under non-vacuum state.

After the selenization of ZIF-67/HMCS composite, the overall morphology does not differ significantly from that prior to the reaction, as shown in Fig. 1a. From the TEM images (Fig. 1b, c), we clearly observe the uniform distribution of ultrafine $CoSe_2$ nanocrystals all over the HMCS, and the numerous mesopores in the HMCS shell are filled with nanocrystals with a diameter of ~ 5 nm. Moreover, large crystals in the central voids of several HMCSs are formed from the selenization of ZIF-67 deposited on the inner surface of the HMCS shell. During selenization, the initially formed small particles in the voids gradually grow via Ostwald ripening as the reaction progresses, thus resulting in the formation of fine $CoSe_2$ crystals [27–29]. High-resolution TEM (HR-TEM, Fig. 1d) analysis shows the tiny nanocrystals enclosed by the amorphous carbon layer derived from the organic linkers of ZIF-67 along with lattice fringes separated by 0.19 nm corresponding to the (211) crystal planes, of orthorhombic $CoSe_2$. Furthermore, the selected-area electron diffraction (SAED) and XRD patterns closely match with the orthorhombic $CoSe_2$ crystal structure (Figs. 1e and S7). The elemental mapping images in Fig. 1f indicate the homogeneous distribution of C, N, Co, and Se elements. The presence of N evidences the formation of N-doped carbon from the organic linkers contained in ZIF-67 after selenization.

In contrast to the morphology of $CoSe_2$@NC/HMCS, irregular-shaped nanocrystals are observed on the surface of the carbon nanospheres in the SEM image of the $CoSe_2$/ HMCS composite (Fig. 2a). Further TEM investigations
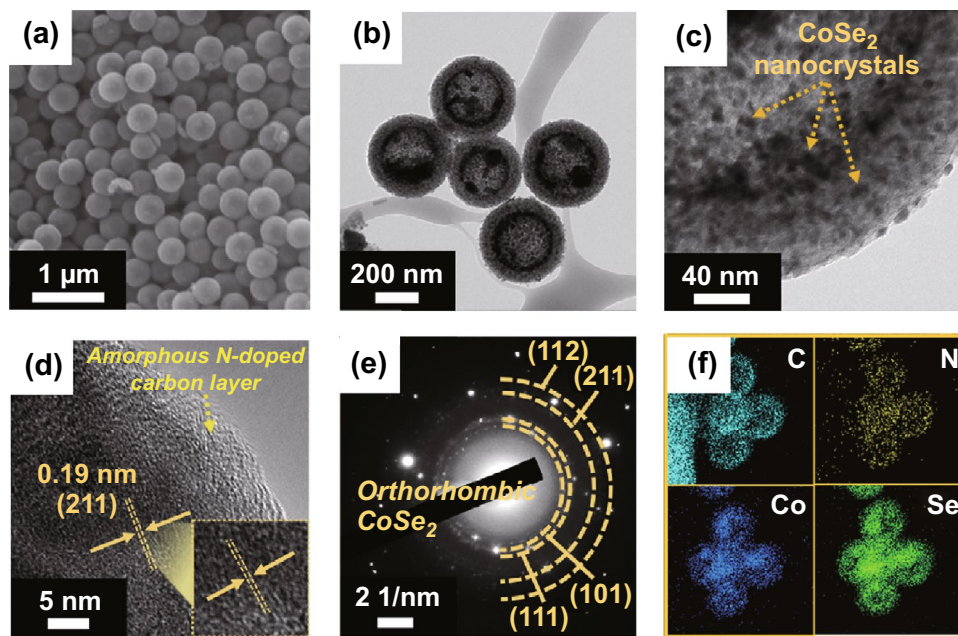
Fig. 1 Morphologies, SAED pattern, and elemental mapping images of CoSe$_2$@NC/HMCS composite formed with 2-methylimidazole: **a** SEM image, **b**, **c** TEM images, **d** HR-TEM image, **e** SAED pattern, and **f** elemental mapping images

(Fig. 2b, c) show the presence of overgrown nanoparticles and nanorods on the outside shell of the HMCS, which are larger than the nanocrystals of the CoSe$_2$@NC/HMCS composite; these crystals and rods may be formed due to Ostwald ripening. Moreover, unlike the CoSe$_2$@NC/HMCS composite, no carbon layer is observed on the surface of
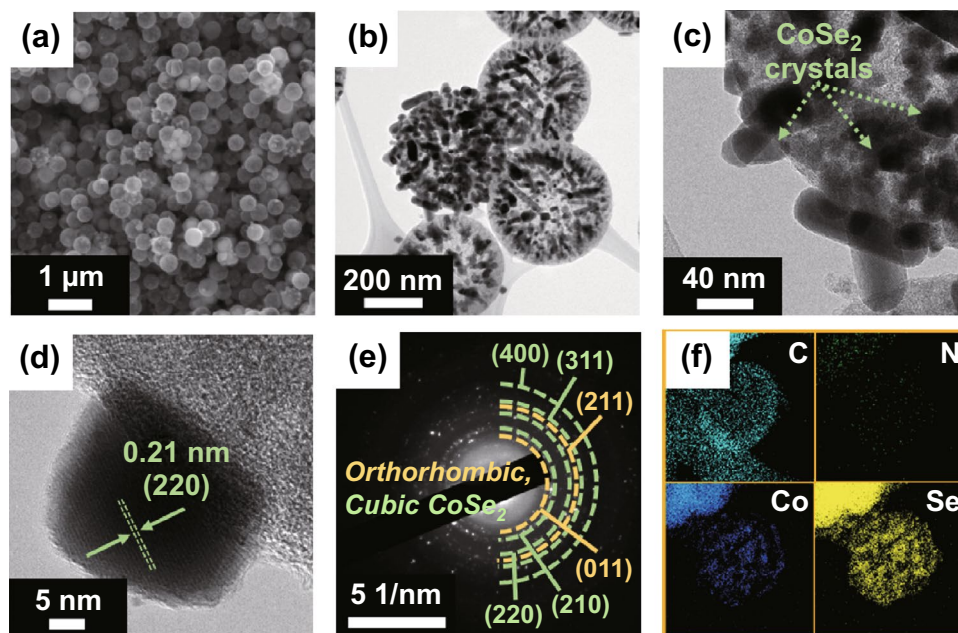

Fig. 2 Morphologies, SAED pattern, and elemental mapping images of CoSe$_2$/HMCS composite formed without 2-methylimidazole: **a** SEM image, **b**, **c** TEM images, **d** HR-TEM image, **e** SAED pattern, and **f** elemental mapping images

the protruded nanocrystals (Fig. 2d). These morphological and structural differences between CoSe₂@NC/HMCS and CoSe₂/HMCS composites prove that ZIF-67 formation can significantly suppress the overgrowth of CoSe₂ nanocrystals during selenization. The SAED and XRD patterns reveal that the nanocrystals in the CoSe₂/HMCS composite are composed of dominant cubic CoSe₂ and minor orthorhombic CoSe₂ crystalline phases (Figs. 2e and S7). From the elemental mapping images (Fig. 2f), there is no signal corresponding to N because of the absence of MOFs.

To study the chemical state of CoSe₂@NC/HMCS composite, we performed the X-ray photoelectron spectroscopy (XPS) measurements (Figs. 3 and S8). From the XPS survey spectrum of the composite, the presence of C, N, O, Co, and Se elements is clearly confirmed, which agrees with the elemental mapping data (Fig. S8). The C 1 s spectrum shows deconvoluted peaks identified at 283.9, 284.9, and 286.2 eV, which are assigned to C=C (sp^2), C–C/C–N (sp^3), and C–O bonds, respectively (Fig. 3a) [14, 30]. For the N 1 s spectrum, three peaks corresponding to pyridinic, pyrrolic, and graphitic N can be confirmed at 397.7, 399.3, and 400.9 eV, respectively (Fig. 3b) [6, 31]. Based on the XPS quantitative

results, the N content in the composite was calculated to be 12.9 at %. Meanwhile, the high-resolution Co 2p spectrum is deconvoluted into many peaks corresponding to Se–Co–Se bonds, cobalt selenites, and satellites (indicated as Sat.) (Fig. 3c) [32, 33]. In a previous report, the presence of peaks corresponding to metal selenites was attributed to the formation of Co–Se–O bonds by the partial surface oxidation of metal selenides [34]. In our case, the high-resolution XPS spectrum of Se 3d can be fitted well with the peaks corresponding to Se 3d₅/₂, Se 3d₃/₂, Se–Se (metalloid Se), Co 3p₃/₂, Co 3p₁/₂, and selenite (Fig. 3d) [14, 35, 36]. The presence of the Se–Se peak indicates that trace metalloid Se remains in the composite. Moreover, the partial surface oxidation of metalloid Se is responsible for the presence of the cobalt selenite peak.

From the thermalgravimetric analysis (TGA) analysis curves of CoSe₂@NC/HMCS and CoSe₂/HMCS composites (Fig. S9a), we observe multiple-step weight losses in the range of 300–600 °C; these can be mainly attributed to the combustion of carbonaceous materials and the oxidation of CoSe₂ nanocrystals. Based on the TG results, the calculated carbon amounts in CoSe₂@NC/HMCS and CoSe₂/
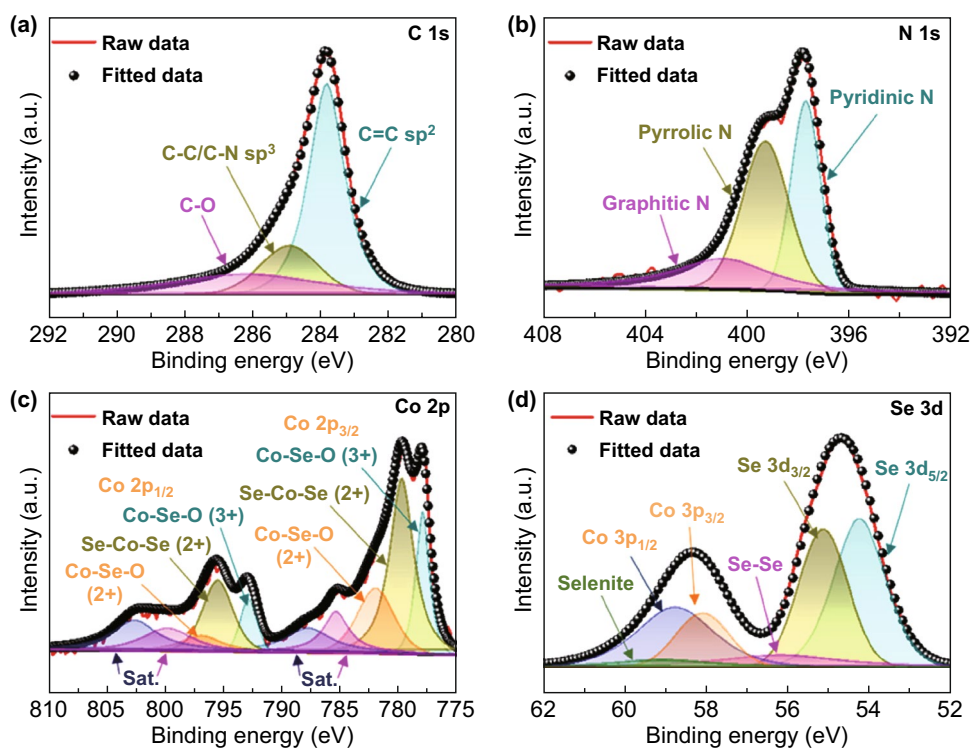
Fig. 3 XPS spectra of CoSe₂@NC/HMCS composite: **a** C 1s, **b** N 1s, **c** Co 2p, and **d** Se 3d

HMCS composites are 64% and 43%, respectively. From the Raman spectroscopy result (Fig. S9b), the I_D/I_G value of CoSe$_2$@NC/HMCS can be determined as 1.05, which indicates defects in the carbon structure, possibly due to N doping and incomplete graphitization. Next, using the Brunauer–Emmett–Teller (BET) analysis (Fig. S9c, d), we calculated the specific surface areas of HMCS, CoSe$_2$@NC/HMCS, and CoSe$_2$/HMCS composites to be 900.1, 77.2, and 46.6 m^2 g^{-1}, respectively. When compared with that of the CoSe$_2$/HMCS composite, the higher surface area of the CoSe$_2$@NC/HMCS composite can be attributed to the presence of porous carbon derived from MOF carbonization. The relatively low surface areas and pore volumes of the composite indicate that CoSe$_2$ nanocrystals are well embedded in the HMCSs.

3.2 K-Ion Storage Mechanism and KIB Performances

Considering that very few studies have focused on CoSe$_2$ embedded in a porous carbon matrix for application as KIB anodes, we investigated the potassium storage mechanism of CoSe$_2$@NC/HMCS based on the ex situ analysis of the initial fully discharged/charged electrodes (Figs. 4 and 5). The TEM images of the fully discharged and charged composite are not as clear as those of the uncycled composite, which could be due to the formation of solid electrolyte interphase (SEI) layers (Fig. 4a, d). From the HR-TEM image and SAED pattern of the electrode in the fully discharged state (Fig. 4b and c, respectively), we clearly observe the formation of tetragonal-phase metallic Co nanoparticles and cubic-phase K$_2$Se. These results indicate that cobalt selenide nanocrystals transform into the corresponding metallic Co nanoparticles, and K$_2$Se is simultaneously formed as a by-product of the chemical reaction between K and Se ions [37]. After full charging, the re-formation of orthorhombic-phase CoSe$_2$ in the composite can be confirmed from the corresponding HR-TEM image and SAED pattern (Fig. 4e, f, respectively); these results indicate that the metallic Co nanoparticles revert back to CoSe$_2$ after the charging process. The ex situ XPS results also support the hypothesized electrochemical storage mechanism of the CoSe$_2$@NC/HMCS electrode [38]. In high-resolution K 2p spectrum, the K$_2$CO$_3$ peak intensity in the fully discharged electrode is higher than that in the fully charged electrode (Fig. 5a, b), which could be due to the partial decomposition of the SEI layer composed of K$_2$CO$_3$ and other by-products [39, 40]. Moreover, from the Co 2p spectrum of the fully discharged electrode, we can clearly identify the deconvoluted peak assigned to metallic Co, which disappears after subsequent charging (Fig. 5c, d). Instead, the Se–Co–Se bond peaks are observed again, which is also supported by the TEM results. The peaks corresponding to cobalt oxides can be ascribed to the partial surface oxidation of cobalt during the measurement.

Figure 6 shows the in situ electrochemical impendence spectroscopy (EIS) analysis results of the CoSe$_2$@NC/HMCS electrode at various voltage levels during the initial
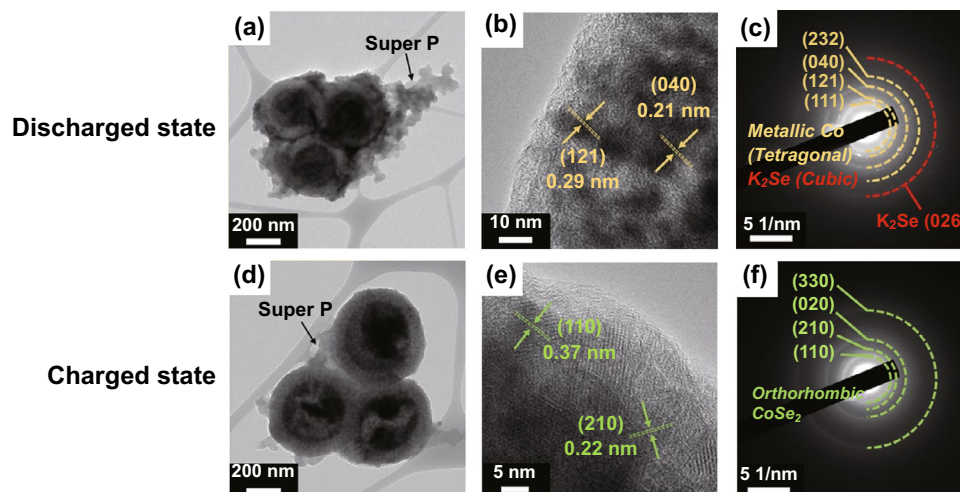

Fig. 4 TEM images and SAED patterns of CoSe$_2$@NC/HMCS composite at the fully **a-c** discharged and **d-f** charged states: **a**, **b**, **d**, **e** TEM images and **c**, **f** SAED patterns
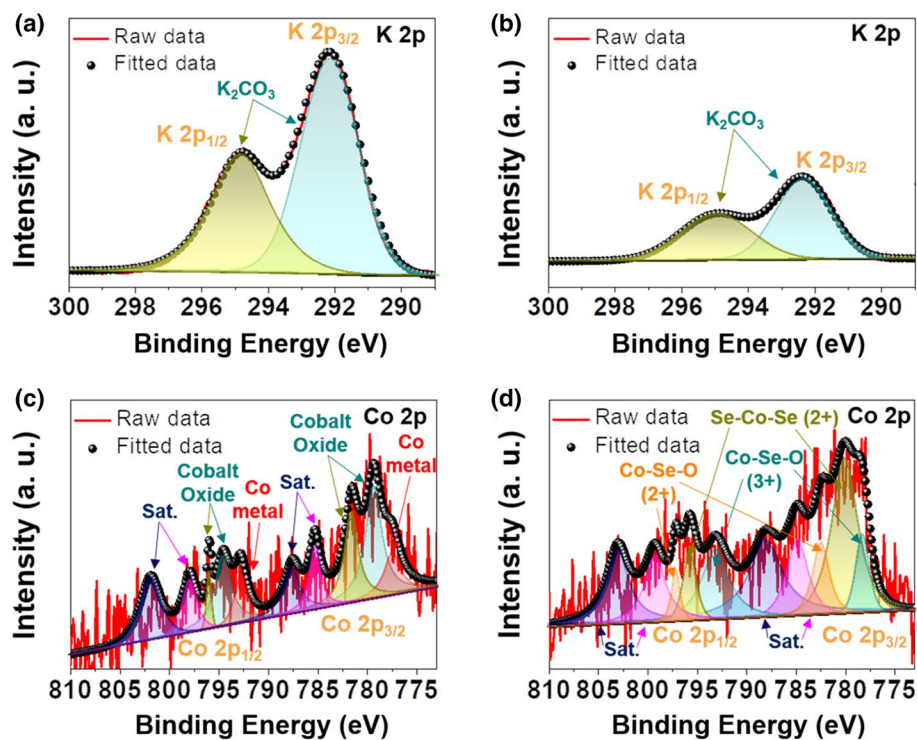
Fig. 5 XPS spectra of CoSe$_2$@NC/HMCS composite: **a**, **b** K 2p, **c**, **d** Co 2p measured after **a**, **c** the initial fully discharged state and **b**, **d** the initial fully charged state

cycling; the EIS results further support the electrochemical mechanism revealed by the cyclic voltammetry (CV) graphs. The Nyquist plots are fitted by the Randles-type equivalent circuit model (Fig. S10) and the plots of the synthesized sample are related to the electrolyte resistance (R_s), interfacial resistances (R_{sei}), charge transfer resistance (R_{ct}), and ion diffusivity, which is drawn as a semicircle and sloping line on the graph. The points in Fig. 6a indicate the preselected
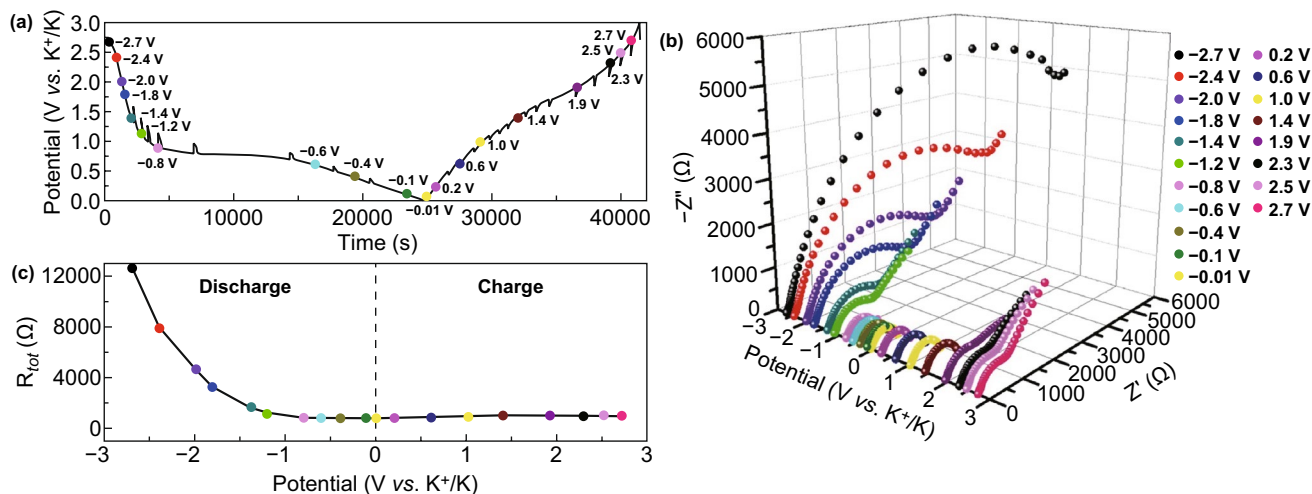

Fig. 6 In situ EIS of CoSe$_2$@NC/HMCS composite: **a** preselected potentials and time curve at a current density of 0.1 A g^{-1}, **b** in situ Nyquist plots at predetermined potentials, and **c** in situ EIS graph (R_{tot} vs. potential) measured at preselected potential during the initial cycle

potentials at which the in situ EIS results were obtained. The Nyquist plots of $CoSe_2$@NC/HMCS at the preselected potentials are depicted in Fig. 6b and the R_{tot} change (related to the sum of R_s, R_{sei}, and R_{ct}) is indicated in Fig. 6c. In the initial discharging process, the R_{tot} value at the predetermined potentials gradually decreases until -0.6 V. In this potential range, the $CoSe_2$@NC/HMCS composite transforms into ultrafine metallic Co and K_2Se, and the potassium bis(fluorosulfonyl) imide (KFSI) in the electrolyte forms a stable SEI layer on the electrode, which can reduce the electrode resistance [41, 42]. However, the R_{tot} value slightly increases during the subsequent charging process until 1.9 V because of the structural stress caused by the phase transformation of metallic Co to $CoSe_2$. Subsequently, R_{tot} continues to decrease until a preselected final potential, which may be associated with complete depotassiation and the decomposition of the reversible SEI layer [43–45]. These results are in good agreement with the above-mentioned ex situ TEM and XPS data (Figs. 4 and 5).

We next applied the CV technique over the potential range of 0.001–3.0 V (vs. K^+/K) to confirm the electrochemical behaviors of $CoSe_2$@NC/HMCS and $CoSe_2$/HMCS electrodes when used as an anode in KIBs. In Fig. 7, the CV graphs of these two anodes for the first, second, and fifth cycles exhibit similar plots that indicate their similar redox reactions. During the initial cathodic sweep, the graph of $CoSe_2$@NC/HMCS shows distinct peaks at ~0.95 and 0.60 V, corresponding to the reduction reaction between K^+ and $CoSe_2$ crystals and the formation of SEI layers, respectively (Fig. 7a) [10, 46]. The peak at ~0.01 V is correlated to the storage of K^+ in the carbon shell [47]. These data are consistent with the results of the ex situ analysis. From the second cycle onward, the CV graph shifts forward due to the formation of tiny $CoSe_2$ particles after the initial cycle. This causes the existing peaks to disappear and two new peaks at ~0.94 and 0.3 V to appear. The peak at ~0.94 V is related to the insertion of K^+ into $CoSe_2$ crystals and that at ~0.3 V is correlated with the conversion reaction with further K^+. In the initial anodic sweep, the three peaks at ~1.89, 1.07, and 0.5 V appear on the CV graph. The peaks at ~1.89 and 1.07 V are related to the transformation of metallic Co nanoparticles and K_2Se into $CoSe_2$ nanocrystals [10, 32]. The peak at ~0.5 V corresponds to the release of K^+ ions that enter the carbon shell during the discharging process [48]. The CV graphs of the second and fifth cycles exhibit a strong
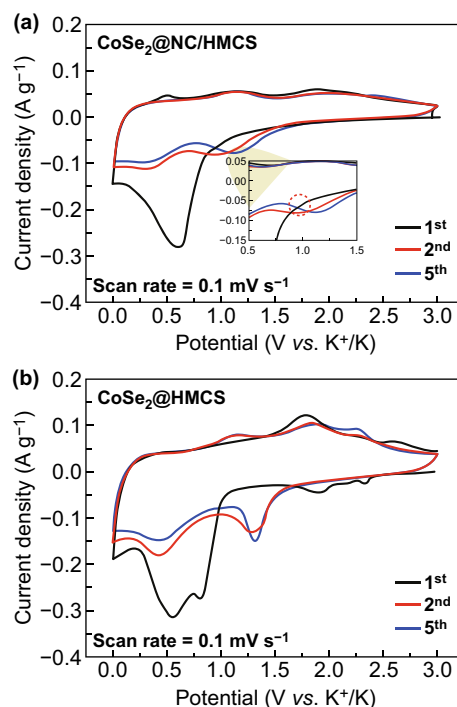
Fig. 7 CV curves of **a** $CoSe_2$@NC/HMCS and **b** $CoSe_2$/HMCS composites obtained at a scan rate of 0.1 mV s^{-1}

overlap, which indicates good electrochemical stability of the $CoSe_2$@NC/HMCS composite. Additionally, the $CoSe_2$/HMCS composite exhibits more distinct peaks in the CV graphs (Fig. 7b) during the charge–discharge process because of the lesser amount of carbonaceous materials relative to that of $CoSe_2$@NC/HMCS, which can be related to the large crystal growth (Fig. 2d).

The electrochemical performances of the $CoSe_2$@NC/HMCS and $CoSe_2$/HMCS composites are shown in Fig. 8. In the initial charge–discharge profiles of both electrodes at a current density of 0.1 A g^{-1} (Fig. 8a), the potential level of the distinct long plateaus is in close agreement with the peak locations in the CV graphs. The initial discharge capacities of $CoSe_2$@NC/HMCS and $CoSe_2$/HMCS composites are 675 and 689 mAh g^{-1}, the initial charging capacities are 448 and 472 mAh g^{-1}, and the initial coulombic efficiencies (CEs) are 66% and 68%, respectively. The low values of initial capacity and CE are mainly related to the formation of the SEI layers by electrolyte decomposition, which is proportional to the electrode surface area [49, 50]. Figure 8b shows the cycle performances of $CoSe_2$@NC/HMCS and $CoSe_2$/HMCS electrodes at a current density 0.1 A g^{-1} for 120 cycles.
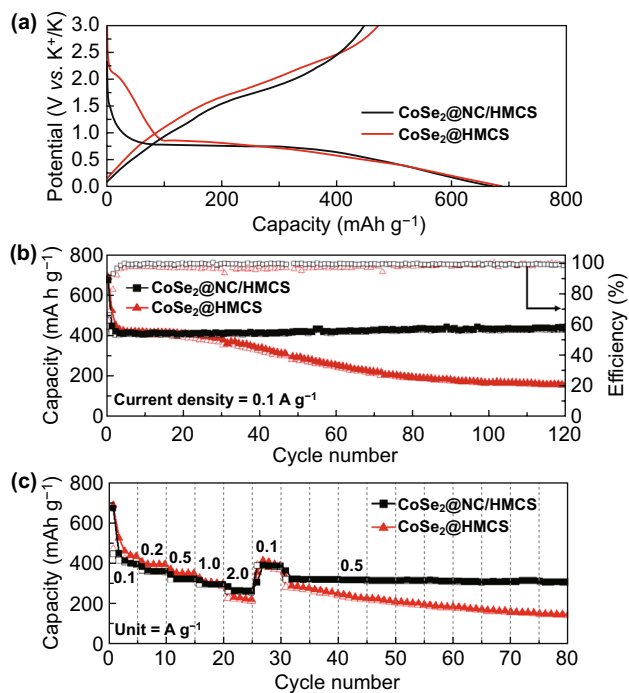
Fig. 8 Electrochemical properties of CoSe$_2$@NC/HMCS and CoSe$_2$/HMCS composites: **a** initial galvanostatic charge–discharge curves, **b** cycle performances at a current density of 0.1 A g^{-1}, and **c** rate performances at various current densities

Over the entire cycle, CoSe$_2$@NC/HMCS shows a high reversible discharge capacity of 442 mAh g^{-1} for 120 cycles with good cycling stability (almost 99% CEs all over the cycling). On the other hand, in the case of the CoSe$_2$/HMCS electrode, a rapid cycle decay is observed after 30 cycles, and eventually, the reversible discharge capacity reaches 160 mAh g^{-1} after 120 cycles. This result indicates that the active material of the electrode could be pulverized due to the large volume expansion during the repeated charging and discharging process. When compared with the CoSe$_2$@NC/HMCS electrode, there is more aggregation between particles, and a thicker SEI layer is formed in CoSe$_2$/HMCS electrode after 100 cycles (Fig. S11a-d). Furthermore, to confirm the electrochemical behavior and K-ion storage contribution of the HMCS in composite, we analyzed the electrochemical properties under the same conditions (Fig. S12a-c). As confirmed in Fig. S12a, HMCS showed the charge–discharge curves of a typical carbonaceous material; there were no apparent plateaus. They also delivered a specific discharge capacity of 208 mAh g^{-1} after 50 cycles at a current density of 0.1 A g^{-1} (Fig. S12b). Despite their low specific capacities,

the synergistic effect between CoSe$_2$ and the conductive HMCS template with mesopores enhanced the capacity of the composite.

Meanwhile, CoSe$_2$@NC/HMCS electrodes were further tested at the ranges of 0.001–2.0 V and 0.001–2.5 V to confirm the effect of potential window range on the electrochemical performance, (Fig. S13a-c). The result exhibited larger initial irreversible capacity and lower reversible capacities than those evaluated at the range of 0.001–3.0 V (Fig. 8), which indicates that the redox reaction may have not occurred sufficiently in the narrow potential range. In light of these results, we make a conclusion that the potential range of 0.001–3.0 V is optimal test condition for CoSe$_2$@NC/HMCS electrodes.

Figure 8c illustrates the rate performance of the two composites in the range of 0.1 to 2.0 A g^{-1}. Although the CoSe$_2$/HMCS composite delivers stable capacities in the low-current–density regime, the capacity begins to gradually decrease from 1.0 A g^{-1}. In addition, when the current density again reverts to 0.5 A g^{-1}, the capacity barely recovers. In contrast, the CoSe$_2$@NC/HMCS composite delivers stable reversible capacities for all current densities, thereby indicating excellent rate capability. The reversible discharge capacities of CoSe$_2$@NC/HMCS composite are 394, 363, 324, 298, and 263 mAh g^{-1} at current densities of 0.1, 0.2, 0.5, 1.0, and 2.0 A g^{-1}, respectively. Moreover, after the current density reverts to low values of 0.1 and 0.5 A g^{-1}, the reversible capacity values are almost completely restored, and good cycling stability is observed for up to 80 cycles. Also, in Fig. S14, the charge–discharge curves of CoSe$_2$@NC/HMCS have similar shapes without significant change at even high current density, which verifies excellent rate performance of CoSe$_2$@NC/HMCS electrode. On the other hand, CoSe$_2$@NC/HMCS composite prepared from the precursors obtained under non-vacuum state showed poor cycling and rate performances (Fig. S15). This could be because CoSe$_2$@NC particles in the composite are not confined within HMCS and are directly exposed to the electrolyte. The aggregation and overgrowth of active material can easily induce structure collapse during repeated cycling process.

To further investigate the influences amount of Co-nitrate in the composite, we added the SEM images and electrochemical performance data of two comparison samples obtained by only adjusting the amount of the Co-nitrate (Figs. S16 and S17). When synthesized by adding only 1/3

times the original amount of Co-nitrate (denoted as $CoSe_2$@NC/HMCS-1/3), there was little difference in the morphology from the $CoSe_2$@NC/HMCS (Fig. S16a). On the other hand, excessive addition of Co-nitrate beyond the absorbing capacity of HMCS template (3 times the original amount, $CoSe_2$@NC/HMCS-3) caused aggregation of $CoSe_2$@NC particles outside of HMCS (Fig. S16b). Additionally, two samples were galvanostatically evaluated as anodes for KIB to confirm their electrochemical properties (Fig. S17). In the cycling performance data, $CoSe_2$@NC/HMCS-1/3 exhibited lower specific capacity than $CoSe_2$@NC/HMCS, whereas $CoSe_2$@NC/HMCS-3 showed higher specific capacity over the entire cycles (Fig. S17a). Meanwhile, despite the highest capacity value of $CoSe_2$@NC/HMCS-3, its rate capability was the worst. At a high current density of 2.0 A g^{-1}, the capacity of $CoSe_2$@NC/HMCS-3 decreased more rapidly compared to other samples, and even after the current density returned to 0.5 A g^{-1}, the capacity of $CoSe_2$/HMCS continued to decrease (Fig. S17b). This could be due to the $CoSe_2$@NC aggregates in the composite that are not confined within HMCS. On the contrary, the other samples showed stable capacity retention throughout all current densities.

These outstanding electrochemical performances of the $CoSe_2$@NC/HMCS composite as KIB anodes can be attributed to its several distinct characteristics. First, the HMCS template and N-doped carbon matrix provide both structural robustness and high electronic conductivity. Second, the unique porous structure consisting of the central void and mesopores can improve the ion diffusion rate and accessibility. Finally, the formation of ultrafine $CoSe_2$ nanocrystals by the "dual confinement system" can effectively alleviate volume expansion during the cycling. In comparison with previously reported metal-selenide-based anodes for KIBs, our $CoSe_2$@NC/HMCS composite exhibits superior electrochemical performances (Table S1), particularly in terms of the reversible capacity and cycling stability.

To examine the electrochemical kinetics, we performed CV measurements of the two electrodes at various scan rates ranging from 0.1 to 2.0 mV s^{-1} (Fig. 9). We note that as the scan speed increases, the cathodic and anodic peaks of the composites gradually deviate from the original peak position due to ohmic resistance (Fig. 9a, b) [9]. The relationship between the current (i) and scan rate (v) can be expressed as follows: $i = av^b$, where both a and b represent empirical values [51, 52]. From Fig. 9c, d, we note that the b values of both electrodes are closer to 1.0, indicating

that the capacitive-controlled process is dominant during the charge–discharge process of the two composites [53]. The correlation graphs between the scan rate and capacitive contribution show that the capacitive contributions of $CoSe_2$@NC/HMCS and $CoSe_2$/HMCS composites gradually increase with the scan rate, and they reach 83% and 89%, respectively, at the scan rate of 2.0 mV s^{-1} (Fig. 9e-h). These high capacitive contributions indicate the quick charge/discharge properties of $CoSe_2$@NC/HMCS and $CoSe_2$/HMCS electrodes. However, despite their high capacitive contribution, the $CoSe_2$/HMCS electrode exhibited a relatively poor rate performance. This is because the rate capability can be influenced not only by several factors related to capacitive behavior, but also by structural change. Therefore, the poor rate capability of $CoSe_2$/HMCS electrode could be due to the structural collapse at high current densities.

Next, we conducted EIS measurements to confirm the resistance value changes of the electrodes for fresh, 1st, 60th, and 100th cycles (Fig. S18). In Fig. S18a, the $CoSe_2$@NC/HMCS electrode exhibits a smaller Nyquist plot than the $CoSe_2$/HMCS electrode in the fresh state, thus indicating that the $CoSe_2$@NC/HMCS electrode has a lower charge transfer resistance. After the initial cycle, the R_{ct} values of the two electrodes drastically decrease, which can be ascribed to the formation of smaller $CoSe_2$ nanocrystals during the cycling and electrode activation by the electrolyte [54, 55]. The R_{ct} value of $CoSe_2$@NC/HMCS electrode gradually decreased as cycle proceeds, indicating the structural robustness of the electrode (Fig. S18b). In contrast, the R_{ct} value of the $CoSe_2$/HMCS electrode at the 100th cycle increases over that at the 60th cycles (Fig. S18c), which could be due to structural collapse during the charge–discharge process. These results are in good agreement with the cycle data shown in Fig. 8b. The relationship between the phase angle ($\omega^{-1/2}$) and impedance (Z') of the two electrodes at the 100th cycle is plotted in Fig. S18d. The cycled $CoSe_2$@NC/HMCS electrode exhibits a smaller slope than that of the cycled $CoSe_2$/HMCS electrode, thereby indicating a faster K^+ ion diffusion rate after 100 cycles [56].

4 Conclusions

In summary, we synthesized a MOF-derived ultrafine $CoSe_2$ nanocrystal@NC matrix confined in hollow mesoporous carbon nanospheres for application as the anode material of
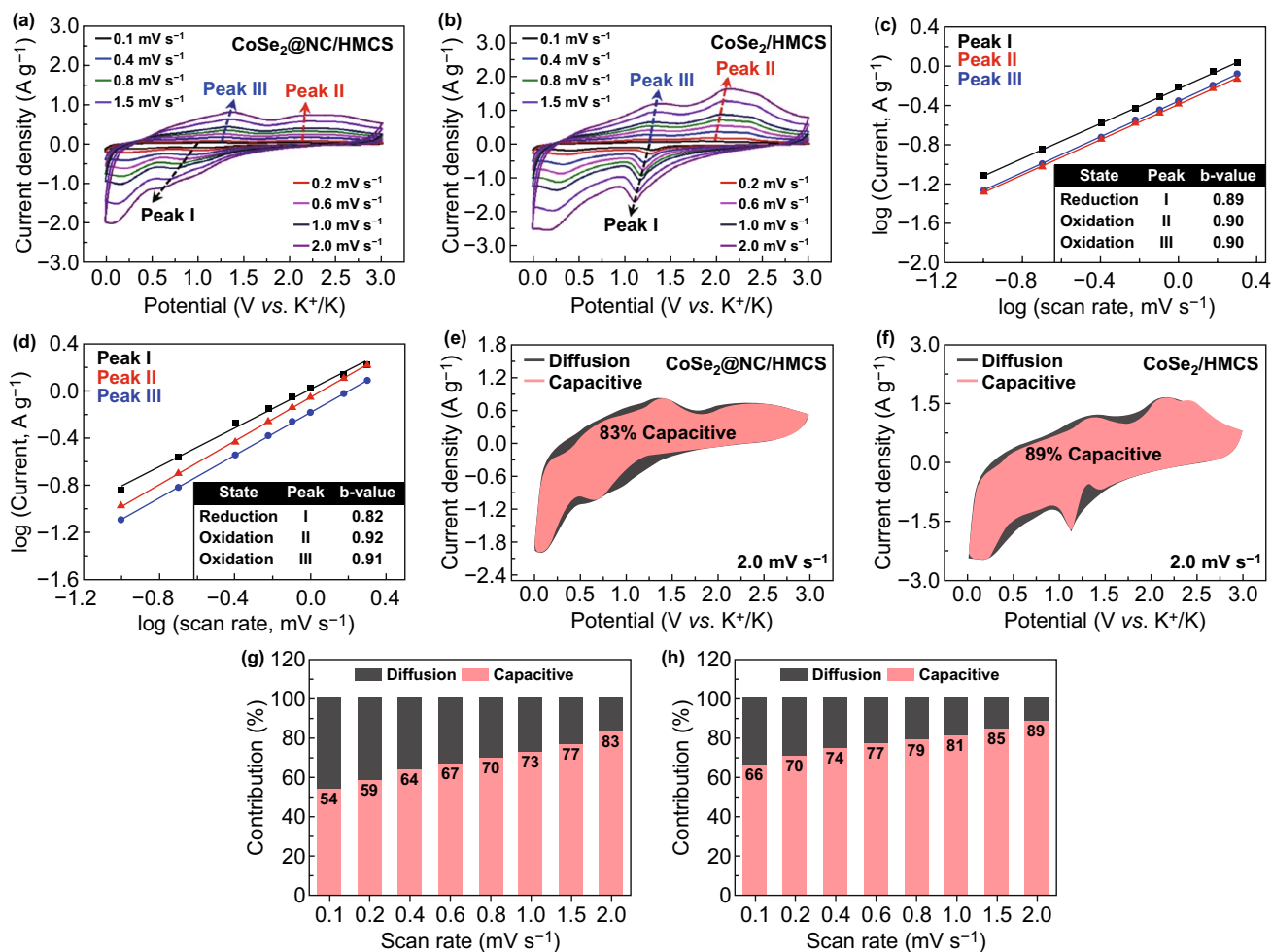
Fig. 9 Kinetic analysis of **a**, **c**, **e**, **g** CoSe$_2$@NC/HMCS and **b**, **d**, **f**, **h** CoSe$_2$/HMCS electrodes for KIBs: **a**, **b** cyclic voltammograms at various sweep rates, **c**, **d** fitted log (peak current) vs. log (scan rate) for peaks corresponding to certain electrochemical reactions, **e**, **f** cyclic voltammograms showing capacitive contribution (colored area) at a scan rate of 2.0 mV s^{-1}, and **g**, **h** capacity contribution at various scan rates

high-performance KIBs. The application of thermal treatment under vacuum state leads to not only the easy infiltration of precursors but also the immediate formation of ZIF-67 nanoparticles within HMCSs. This novel approach can effectively suppress the overgrowth of CoSe$_2$ nanocrystals during the subsequent selenization step, thereby resulting in the formation of ultrafine CoSe$_2$ nanocrystals embedded in the N-doped carbon matrix and their homogeneous distribution within the HMCSs. These unique features ensure that the CoSe$_2$@NC/HMCS composite can not only provide sufficient channels for electron and ion transfers but also alleviate the volume expansion of CoSe$_2$ nanocrystals during electrochemical reactions. Accordingly, the CoSe$_2$@NC/HMCS composite exhibited a high reversible capacity,

long-term cycling stability, and excellent rate capabilities when used as an anode for KIBs. Our strategy for synthesizing uniquely structured metal selenide/carbon composite can be extended to other novel electrodes for high-performance energy storage applications.

References

1. M. Ma, S. Zhang, Y. Yao, H. Wang, H. Huang et al., Heterostructures of 2D molybdenum dichalcogenide on 2D nitrogen-doped carbon: superior potassium-ion storage and insight into potassium storage mechanism. Adv. Mater. **32**(22), 2000958 (2020). https://doi.org/10.1002/adma.202000958

2. J. Dong, J. Liao, X. He, Q. Hu, Y. Yu, C. Chen, Graphene encircled $KFeSO_4F$ cathode composite for high energy density potassium-ion batteries. Chem. Commun. **56**, 10050–10053 (2020). https://doi.org/10.1039/D0CC03795H

3. C. Wang, B. Zhang, H. Xia, L. Cao, B. Luo et al., Composition and architecture design of double-shelled $Co_{0.85}Se_{1−x}S_x@$ carbon/graphene hollow polyhedron with superior alkali (Li, Na, K)-ion storage. Small **16**(17), 1905853 (2020). https://doi.org/10.1002/smll.201905853

4. H. Tian, X. Yu, H. Shao, L. Dong, Y. Chen et al., Unlocking few-layered ternary chalcogenides for high-performance potassium-ion storage. Adv. Energy Mater. **9**(29), 1901560 (2019). https://doi.org/10.1002/aenm.201901560

5. J. Chu, Q. Yu, D. Yang, L. Xing, C.-Y. Lao et al., Thickness-control of ultrathin bimetallic Fe–Mo selenide@N-doped carbon core/shell "nano-crisps" for high-performance potassium-ion batteries. Appl. Mater. Today **13**, 344–351 (2018). https://doi.org/10.1016/j.apmt.2018.10.004

6. C.A. Etogo, H. Huang, H. Hong, G. Liu, L. Zhang, Metal–organic-frameworks-engaged formation of $Co_{0.85}Se@C$ nanoboxes embedded in carbon nanofibers film for enhanced potassium-ion storage. Energy Storage Mater. **24**, 167–176 (2020). https://doi.org/10.1016/j.ensm.2019.08.022

7. Y. He, L. Wang, C. Dong, C. Li, X. Ding, Y. Qian, L. Xu, In-situ rooting ZnSe/N-doped hollow carbon architectures as high-rate and long-life anode materials for half/full sodium-ion and potassium-ion batteries. Energy Storage Mater. **23**, 35–45 (2019). https://doi.org/10.1016/j.ensm.2019.05.039

8. Q. Yu, B. Jiang, J. Hu, C.Y. Lao, Y. Gao et al., Metallic octahedral $CoSe_2$ threaded by N-doped carbon nanotubes: a flexible framework for high-performance potassium-ion batteries. Adv. Sci. **5**(10), 1800782 (2018). https://doi.org/10.1002/advs.201800782

9. J. Wang, B. Wang, X. Liu, J. Bai, H. Wang, G. Wang, Prussian blue analogs (PBA) derived porous bimetal (Mn, Fe) selenide with carbon nanotubes as anode materials for sodium and potassium ion batteries. Chem. Eng. J. **382**, 123050 (2020). https://doi.org/10.1016/j.cej.2019.123050

10. G. Suo, J. Zhang, D. Li, Q. Yu, W. Wang et al., N-doped carbon/ultrathin 2D metallic cobalt selenide core/sheath flexible framework bridged by chemical bonds for high-performance potassium storage. Chem. Eng. J. **388**, 124396 (2020). https://doi.org/10.1016/j.cej.2020.124396

11. L. Yang, W. Hong, Y. Tian, G. Zou, H. Hou, W. Sun, X. Ji, Heteroatom-doped carbon inlaid with Sb_2X_3 (x = S, Se) nanodots for high-performance potassium-ion batteries. Chem. Eng. J. **385**, 123838 (2020). https://doi.org/10.1016/j.cej.2019.123838

12. X. Xu, T. Yang, Q. Zhang, W. Xia, Z. Ding et al., Ultrahigh capacitive deionization performance by 3D interconnected MOF-derived nitrogen-doped carbon tubes. Chem. Eng. J. **390**, 124493 (2020). https://doi.org/10.1016/j.cej.2020.124493

13. Y. Fu, Q. Wei, G. Zhang, X. Wang, J. Zhang et al., High-performance reversible aqueous Zn-ion battery based on porous MnO_x nanorods coated by MOF-derived N-doped carbon. Adv. Energy Mater. **8**(26), 1801445 (2018). https://doi.org/10.1002/aenm.201801445

14. S.H. Yang, S.-K. Park, Y.C. Kang, Mesoporous $CoSe_2$ nanoclusters threaded with nitrogen-doped carbon nanotubes for high-performance sodium-ion battery anodes. Chem. Eng. J. **370**, 1008–1018 (2019). https://doi.org/10.1016/j.cej.2019.03.263

15. F. Han, T. Lv, B. Sun, W. Tang, C. Zhang, X. Li, In situ formation of ultrafine CoS_2 nanoparticles uniformly encapsulated in N/S-doped carbon polyhedron for advanced sodium-ion batteries. RSC Adv. **7**(49), 30699–30706 (2017). https://doi.org/10.1039/C7RA03628K

16. Y. Zhang, A. Pan, L. Ding, Z. Zhou, Y. Wang et al., Nitrogen-doped yolk–shell-structured CoSe/C dodecahedra for high-performance sodium ion batteries. ACS Appl. Mater. Interfaces **9**(4), 3624–3633 (2017). https://doi.org/10.1021/acsami.6b13153

17. Y.M. Chen, L. Yu, X.W. Lou, Hierarchical tubular structures composed of Co_3O_4 hollow nanoparticles and carbon nanotubes for lithium storage. Angew. Chem. Int. Ed. **55**(20), 5990–5993 (2016). https://doi.org/10.1002/anie.201600133

18. Q. Deng, S. Feng, P. Hui, H. Chen, C. Tian, R. Yang, Y. Xu, Exploration of low-cost microporous Fe(III)-based organic framework as anode material for potassium-ion batteries. J. Alloys Compd. **830**, 154714 (2020). https://doi.org/10.1016/j.jallcom.2020.154714

19. C. Li, X. Hu, B. Hu, Cobalt(II) dicarboxylate-based metal-organic framework for long-cycling and high-rate potassium-ion battery anode. Electrochim. Acta **253**, 439–444 (2017). https://doi.org/10.1016/j.electacta.2017.09.090

20. J. Yang, Z. Ju, Y. Jiang, Z. Xing, B. Xi, J. Feng, S. Xiong, Enhanced capacity and rate capability of nitrogen/oxygen dual-doped hard carbon in capacitive potassium-ion storage.

Adv. Mater. **30**(4), 1700104 (2018). https://doi.org/10.1002/adma.201700104

21. Y. Zhang, N. Zhang, J. Chen, T. Zhang, W. Ge et al., Preparation and lithium storage properties of C@TiO$_2$/3D carbon hollow sphere skeleton composites. J. Alloys Compd. **815**, 152511 (2020). https://doi.org/10.1016/j.jallcom.2019.152511

22. X. Zhang, C. Shen, H. Wu, Y. Han, X. Wu et al., Filling few-layer ReS$_2$ in hollow mesoporous carbon spheres for boosted lithium/sodium storage properties. Energy Storage Mater. **26**, 457–464 (2020). https://doi.org/10.1016/j.ensm.2019.11.019

23. G. Lee, W. Na, J. Kim, S. Lee, J. Jang, Improved electrochemical performances of MOF-derived Ni–Co layered double hydroxide complexes using distinctive hollow-in-hollow structures. J. Mater. Chem. A **7**(29), 17637–17647 (2019). https://doi.org/10.1039/C9TA05138D

24. Y. Zhang, X. Bo, C. Luhana, H. Wang, M. Li, L. Guo, Facile synthesis of a Cu-based MOF confined in macroporous carbon hybrid material with enhanced electrocatalytic ability. Chem. Commun. **49**(61), 6885–6887 (2013). https://doi.org/10.1039/C3CC43292K

25. W. Li, R. Zhao, K. Zhou, C. Shen, X. Zhang et al., Cage-structured M$_x$P$_y$@CNCs (M = Co and Zn) from MOF confined growth in carbon nanocages for superior lithium storage and hydrogen evolution performance. J. Mater. Chem. A **7**(14), 8443–8450 (2019). https://doi.org/10.1039/C9TA00054B

26. H. Zhang, O. Noonan, X. Huang, Y. Yang, C. Xu, L. Zhou, C. Yu, Surfactant-free assembly of mesoporous carbon hollow spheres with large tunable pore sizes. ACS Nano **10**(4), 4579–4586 (2016). https://doi.org/10.1021/acsnano.6b00723

27. Q. An, Q. Wei, L. Mai, J. Fei, X. Xu et al., Supercritically exfoliated ultrathin vanadium pentoxide nanosheets with high rate capability for lithium batteries. Phys. Chem. Chem. Phys. **15**(39), 16828–16833 (2013)

28. C. Han, F. Liu, J. Liu, Q. Li, J. Meng et al., Facile template-free synthesis of uniform carbon-confined V$_2$O$_5$ hollow spheres for stable and fast lithium storage. J. Mater. Chem. A **6**(15), 6220–6224 (2018). https://doi.org/10.1039/C3CP52624K

29. D. Zhang, Y. Zhang, Y. Luo, Y. Zhang, X. Li et al., High-performance asymmetrical supercapacitor composed of rGO-enveloped nickel phosphite hollow spheres and N/S Co-doped rGo aerogel. Nano Res. **11**(3), 1651–1663 (2018). https://doi.org/10.1007/s12274-017-1780-3

30. V.A. Agubra, L. Zuniga, D. Flores, H. Campos, J. Villarreal, M. Alcoutlabi, A comparative study on the performance of binary SnO$_2$/NiO/C and Sn/C composite nanofibers as alternative anode materials for lithium ion batteries. Electrochim. Acta **224**, 608–621 (2017). https://doi.org/10.1016/j.electacta.2016.12.054

31. X. Liu, X. Li, J. Yu, Y. Sun, Ultrasmall Sn nanoparticles embedded in N-doped carbon nanospheres as long cycle life anode for lithium ion batteries. Mater. Lett. **223**, 203–206 (2018). https://doi.org/10.1016/j.matlet.2018.04.043

32. S.-K. Park, J.K. Kim, Y.C. Kang, Excellent sodium-ion storage performances of CoSe$_2$ nanoparticles embedded within

N-doped porous graphitic carbon nanocube/carbon nanotube composite. Chem. Eng. J. **328**, 546–555 (2017). https://doi.org/10.1016/j.cej.2017.07.079

33. H. Chen, S. Chen, M. Fan, C. Li, D. Chen, G. Tian, K. Shu, Bimetallic nickel cobalt selenides: a new kind of electroactive material for high-power energy storage. J. Mater. Chem. A **3**(47), 23653–23659 (2015). https://doi.org/10.1039/C5TA08366D

34. Q. Zheng, X. Cheng, H. Li, Microwave synthesis of high activity FeSe$_2$/C catalyst toward oxygen reduction reaction. Catalysts **5**(3), 1079–1091 (2015). https://doi.org/10.3390/catal5031079

35. C. Xia, Q. Jiang, C. Zhao, M.N. Hedhili, H.N. Alshareef, Selenide-based electrocatalysts and scaffolds for water oxidation applications. Adv. Mater. **28**(1), 77–85 (2016). https://doi.org/10.1002/adma.201503906

36. H. Li, D. Gao, X. Cheng, Simple microwave preparation of high activity Se-rich CoSe$_2$/C for oxygen reduction reaction. Electrochim. Acta **138**, 232–239 (2014). https://doi.org/10.1016/j.electacta.2014.06.065

37. G. Ma, C. Li, F. Liu, M.K. Majeed, Z. Feng et al., Metal-organic framework-derived Co$_{0.85}$Se nanoparticles in N-doped carbon as a high-rate and long-lifespan anode material for potassium ion batteries. Mater. Today Energy **10**, 241–248 (2018). https://doi.org/10.1016/j.mtener.2018.09.013

38. K. Zou, P. Cai, Y. Tian, J. Li, C. Liu et al., Voltage-induced high-efficient in situ presodiation strategy for sodium ion capacitors. Small Methods **4**(3), 1900763 (2020). https://doi.org/10.1002/smtd.201900763

39. Y. Yi, Z. Sun, C. Li, Z. Tian, C. Lu et al., Designing 3D biomorphic nitrogen-doped MoSe$_2$/graphene composites toward high-performance potassium-ion capacitors. Adv. Funct. Mater. **30**(4), 1903878 (2020). https://doi.org/10.1002/adfm.201903878

40. B. Tian, W. Tang, C. Su, Y. Li, Reticular V$_2$O$_5$·0.6H$_2$O xerogel as cathode for rechargeable potassium ion batteries. ACS Appl. Mater. Interfaces **10**(1), 642–650 (2018). https://doi.org/10.1021/acsami.7b15407

41. Y. Tang, Y. Zhang, X. Rui, D. Qi, Y. Luo et al., Conductive inks based on a lithium titanate nanotube gel for high-rate lithium-ion batteries with customized configuration. Adv. Mater. **28**(8), 1567–1576 (2016). https://doi.org/10.1002/adma.201505161

42. G.D. Park, J.-K. Lee, Y.C. Kang, Electrochemical reaction mechanism of amorphous iron selenite with ultrahigh rate and excellent cyclic stability performance as new anode material for lithium-ion batteries. Chem. Eng. J. **389**, 124350 (2020). https://doi.org/10.1016/j.cej.2020.124350

43. S.H. Lim, G.D. Park, D.S. Jung, J.-H. Lee, Y.C. Kang, Towards an efficient anode material for Li-ion batteries: understanding the conversion mechanism of nickel hydroxy chloride with Li-ions. J. Mater. Chem. A **8**, 1939–1946 (2020). https://doi.org/10.1039/C9TA12321K

44. H. Sun, G. Xin, T. Hu, M. Yu, D. Shao, X. Sun, J. Lian, High-rate lithiation-induced reactivation of mesoporous hollow

spheres for long-lived lithium-ion batteries. Nat. Commun. **5**, 4526 (2014). https://doi.org/10.1038/ncomms5526

45. G.D. Park, Y.C. Kang, Enhanced li-ion storage performance of novel tube-in-tube structured nanofibers with hollow metal oxide nanospheres covered with a graphitic carbon layer. Nanoscale **12**, 8404–8414 (2020). https://doi.org/10.1039/D0NR00592D

46. H. Hu, J. Zhang, B. Guan, X.W. Lou, Unusual formation of CoSe@carbon nanoboxes, which have an inhomogeneous shell, for efficient lithium storage. Angew. Chem. Int. Ed. **55**(33), 9514–9518 (2016). https://doi.org/10.1002/anie.201603852

47. Y. Liu, C. Yang, Y. Li, F. Zheng, Y. Li et al., FeSe$_2$/nitrogen-doped carbon as anode material for potassium-ion batteries. Chem. Eng. J. **393**, 124590 (2020). https://doi.org/10.1016/j.cej.2020.124590

48. P. Xiong, X. Zhao, Y. Xu, Nitrogen-doped carbon nanotubes derived from metal–organic frameworks for potassium-ion battery anodes. Chemsuschem **11**(1), 202–208 (2018). https://doi.org/10.1002/cssc.201701759

49. T. Wang, H. Li, S. Shi, T. Liu, G. Yang, Y. Chao, F. Yin, 2D film of carbon nanofibers elastically astricted MnO microparticles: a flexible binder-free anode for highly reversible lithium ion storage. Small **13**(20), 1604182 (2017). https://doi.org/10.1002/smll.201604182

50. D. Jin, X. Yang, Y. Ou, M. Rao, Y. Zhong et al., Thermal pyrolysis of Si@ZIF-67 into Si@N-doped CNTs towards highly stable lithium storage. Sci. Bull. **65**(6), 452–459 (2020). https://doi.org/10.1016/j.scib.2019.12.005

51. Y. Fang, R. Hu, B. Liu, Y. Zhang, K. Zhu et al., MXene-derived TiO$_2$/reduced graphene oxide composite with an enhanced capacitive capacity for Li-ion and K-ion batteries. J. Mater. Chem. A **7**(10), 5363–5372 (2019). https://doi.org/10.1039/C8TA12069B

52. Z. Kangyu, P. Cai, B. Wang, C. Liu, J. Li et al., Insights into enhanced capacitive behavior of carbon cathode for lithium ion capacitors: the coupling of pore size and graphitization engineering. Nano-Micro Lett. **12**, 121 (2020). https://doi.org/10.1007/s40820-020-00458-6

53. Y. Fang, D. Luan, Y. Chen, S. Gao, X.W. Lou, Rationally designed three-layered Cu$_2$S@ carbon@MoS$_2$ hierarchical nanoboxes for efficient sodium storage. Angew. Chem. Int. Ed. **59**(18), 7178–7183 (2020). https://doi.org/10.1002/anie.201915917

54. S.-K. Park, Y.C. Kang, MOF-templated N-doped carbon-coated CoSe$_2$ nanorods supported on porous CNT microspheres with excellent sodium-ion storage and electrocatalytic properties. ACS Appl. Mater. Interfaces **10**(20), 17203–17213 (2018). https://doi.org/10.1021/acsami.8b03607

55. J.H. Choi, S.-K. Park, Y.C. Kang, N-doped carbon coated Ni-Mo sulfide tubular structure decorated with nanobubbles for enhanced sodium storage performance. Chem. Eng. J. **383**, 123112 (2020). https://doi.org/10.1016/j.cej.2019.123112

56. J.K. Kim, S.-K. Park, J.-S. Park, Y.C. Kang, Uniquely structured composite microspheres of metal sulfides and carbon with cubic nanorooms for highly efficient anode materials for sodium-ion batteries. J. Mater. Chem. A **7**(6), 2636–2645 (2019). https://doi.org/10.1039/C8TA11481A